SPATIALLY VARIABLE COAL SLOPE STABILITY ANALYSIS USING IMAGE-BASED SCALED BOUNDARY FINITE ELEMENT METHOD

Dakshith Ruvin Wijesinghe[1*], Ashley Dyson[2], Greg You[1], Manoj Khandelwal[1], Ean Tat Ooi[1]

[1] School of Engineering, Information Technology and Physical Sciences Federation University, Ballarat, 3350, Australia

[2]School of Engineering, University of Tasmania, Hobart, 7005, Australia
[*]Corresponding Author – dakshith@students.federation.edu.au

Key Words: Slope stability, SBFEM, spatial variation, image-based meshing

Abstract. *Slope stability analysis is a challenging task when complex stratigraphies, complex geometries and spatially variably soil parameters are considered. Numerical methods, such as the finite element method are commonly used in slope stability analyses, however, these methods require significant user input when meshing geometries consisting of heterogeneous and spatially variable materials. This paper presents a numerical technique combining the scaled boundary finite element method and image-based meshing for slope stability analysis. The inputs for the analyses require images detailing the stratigraphy and the spatial variation of the material properties. Quadtree decomposition is applied to simultaneously generate meshes and consider the spatial variation of material properties directly from the images through a mapping technique. The stability of slopes is analysed assuming an elastoplastic Mohr-Coulomb constitutive model for the soil. The shear strength reduction technique is applied to evaluate the shear reduction factor iteratively to define the factor of safety of the slope. Coal slopes at Yallourn open-pit mine, Victoria, Australia was considered, forming the basis of a case study to demonstrate the applicability of the presented method.*

1 INTRODUCTION

Slope instability in open-pit mining is a critical problem as it can cause fatal disasters, impacting human life and the economy. Hence, considerable attention has been given to slope stability analysis, with various methods often categorised into numerical methods [1-3] and Limit Equilibrium (LE) methods [4-6]. Numerical methods such as the finite element method have become commonplace in slope stability analysis as numerical methods do not require assumptions such as material isotropy, linear elastic perfectly plastic materials, and quasi-static loading regimes compared to LE. The stability of a slope can be affected by the factors such as groundwater conditions, soil properties and their variation, slope geometry and distribution of discontinuities. However, traditional slope stability analysis is performed on a homogeneous slope [1]. In reality, soil and rock properties are spatially variable and are often reflected in more conservative factors of safety [7].

Slope stability analysis integrating real conditions is still a challenge due to complex

geological structures. In recent times, Cho [8] combined LEM with random field theory to integrate spatial variable parameters in slope stability. The Random Finite Element Method (RFEM) [9, 10] has become a popular, more accurate method that widely used in slope stability analysis, mapping spatially variable characteristics to a finite element mesh. RFEM is a more complicated process as it requires complex mesh generation, mapping spatial variable properties. Additionally, capturing complex geological features on a finite element mesh can be a complicated, time-consuming process that requires human involvement.

To overcome the difficulties of modelling slope complexities and finite element limitations, an image-based numerical method combining the Scaled Boundary Finite Element Method (SBFEM) is introduced in this research. SBFEM is capable of capturing complex geometries as it allows for integration of any size and shape of elements that satisfy scaling features in the mesh [11]. Further, SBFEM can handle hanging nodes in a mesh, while image-based mesh generation can be easily implemented with quadtree mesh generation. Hence, it is fully automatic and easily captured spatial variation of material parameters.

This paper begins by introducing brief SBFEM formulations for elastoplastic analysis. Thereafter, image-based mesh generation for spatial variable simulation is presented. Finally, a case study of the spatially variable slope of the an Australian open-pit mine is considered as an application.

2 METHODOLOGY

2.1 SBFEM formulation

As shown in Figure 1, any number of sides polygons can be considered for SBFEM if all nodes of the polygon can be visible from a point in the domain called a scaling centre. The polygon boundary is discretised with line elements and assigned local coordinates of $-1 \leq \eta \leq 1$ while radial coordinates from the scaling centre is assigned local coordinates of $0 \leq \xi \leq 1$ as shown in Figure 1.
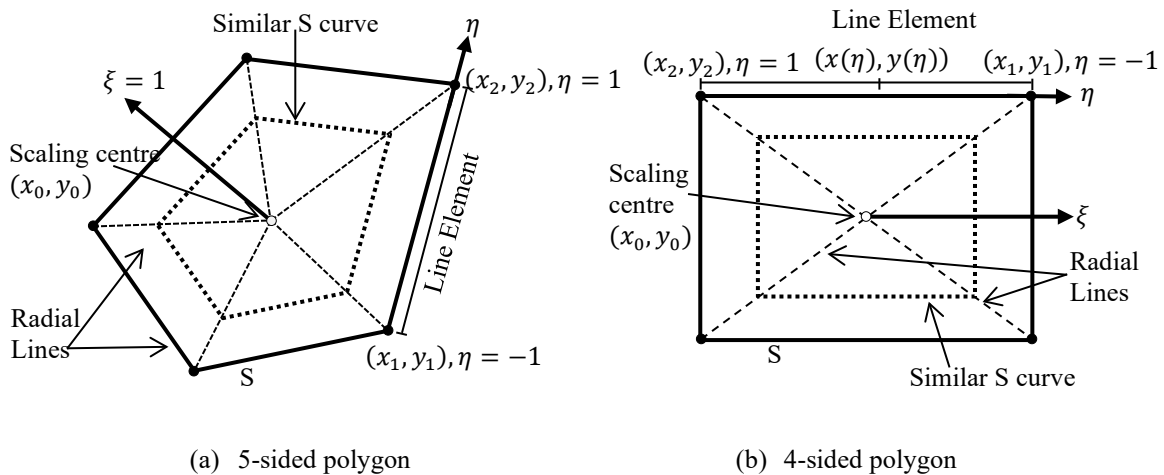

(a) 5-sided polygon (b) 4-sided polygon

Figure 1: Polygon modeled with SBFEM

Considering triangles created between scaling centre and line elements, coordinates of any point in the domain can be expressed in the form of scaled boundary formulation as,

$$x_\eta(\eta) = x_0 + \xi N(\eta)x_b \qquad and \qquad y_\eta(\eta) = y_0 + \xi N(\eta)y_b \qquad (1)$$

where x_0 and y_0 are nodal coordinates of the domain and $N(\eta)$ is the shape functions of line elements of the domain.

The displacement field of any point in the domain can be expressed as,

$$\boldsymbol{u}(\xi,\eta) = \mathbb{N}_u(\eta)\boldsymbol{u}(\xi) \qquad (2)$$

where

$$\mathbb{N}_u(\eta) = \begin{bmatrix} N_1(\eta) & 0 & N_2(\eta) & 0 & \cdots & N_n(\eta) & 0 \\ 0 & N_1(\eta) & 0 & N_2(\eta) & \cdots & 0 & N_n(\eta) \end{bmatrix} \qquad (3)$$

Hence, the strain field of any point in the domain can be transformed in the form of scaled boundary finite element [12] as

$$\epsilon(\xi,\eta) = \mathbb{B}_1(\eta)\boldsymbol{u}(\xi)_{,\xi} + \frac{1}{\xi}\mathbb{B}_2(\eta)\boldsymbol{u}(\xi) \qquad (4)$$

where $\mathbb{B}_1(\eta) = \boldsymbol{b}_1(\eta)\mathbb{N}_u(\eta)$ and $\mathbb{B}_2(\eta) = \boldsymbol{b}_2(\eta)\mathbb{N}_u(\eta)_{,\eta}$ are the strain-displacement [11] with

$$\boldsymbol{b}_1(\eta) = \frac{1}{|\boldsymbol{J}(\eta)|}\begin{bmatrix} y_\eta(\eta)_{,\eta} & 0 \\ 0 & -x_\eta(\eta)_{,\eta} \\ -x_\eta(\eta)_{,\eta} & y_\eta(\eta)_{,\eta} \end{bmatrix} \qquad and \qquad \boldsymbol{b}_2(\eta) = \frac{1}{|\boldsymbol{J}(\eta)|}\begin{bmatrix} -y_\eta(\eta) & 0 \\ 0 & x_\eta(\eta) \\ x_\eta(\eta) & -y_\eta(\eta) \end{bmatrix} \qquad (5)$$

where

$$[\boldsymbol{J}(\eta)] = \begin{bmatrix} \dfrac{\partial x}{\partial \xi} & \dfrac{\partial y}{\partial \eta} \\ \dfrac{\partial x}{\partial \xi} & \dfrac{\partial y}{\partial \eta} \end{bmatrix} = \begin{bmatrix} x_\eta(\eta) & y_\eta(\eta) \\ x_\eta(\eta)_{,\eta} & y_\eta(\eta)_{,\eta} \end{bmatrix} \qquad (6)$$

Considering the virtual work principle [13], the equilibrium condition of a polygon can be derived as

$$\mathbb{E}_0\xi^2\boldsymbol{u}(\xi)_{,\xi\xi} + (\mathbb{E}_0 - \mathbb{E}_1 + \mathbb{E}_1^T)\xi\boldsymbol{u}(\xi)_{,\xi} - \mathbb{E}_2\boldsymbol{u}(\xi) = 0 \qquad (7)$$

where

$$\mathbb{E}_0 = \int_{-1}^{+1} \mathbb{B}_1^T(\eta)\boldsymbol{D}\mathbb{B}_1(\eta)\,|\boldsymbol{J}(\eta)|d\eta \qquad (8)$$

$$\mathbb{E}_1 = \int_{-1}^{+1} \mathbb{B}_2^T(\eta)\boldsymbol{D}\mathbb{B}_1(\eta)\,|\boldsymbol{J}(\eta)|d\eta \qquad (9)$$

3

$$\mathbb{E}_2 = \int_{-1}^{+1} \mathbb{B}_2^T(\eta) \boldsymbol{D} \mathbb{B}_2(\eta) |\boldsymbol{J}(\eta)| d\eta \tag{10}$$

The solution of $\boldsymbol{u}(\xi)$ for the bounded domain can be expressed as [11]

$$\boldsymbol{u}(\xi) = \boldsymbol{\psi}_u \xi^{-S_n} \boldsymbol{c}_n \tag{11}$$

where $\boldsymbol{S}_n$ is a Schur matrix containing negative eigenvalues along the diagonal and $\boldsymbol{\psi}_u$ is a corresponding transformation matrix. These matrixes can be obtained by solving the Hamiltonian matrix $\mathbb{Z}$ with Schur decomposition. The Hamiltonian matrix is defined as

$$\mathbb{Z} = \begin{bmatrix} \mathbb{E}_0^{-1}\mathbb{E}_1^T & -\mathbb{E}_0^{-1} \\ \mathbb{E}_1\mathbb{E}_0^{-1}\mathbb{E}_1^T - \mathbb{E}_2 & -\mathbb{E}_1\mathbb{E}_0^{-1} \end{bmatrix} \tag{12}$$

Applying the Schur decomposition results in

$$\mathbb{Z}\begin{bmatrix} \boldsymbol{\psi}_u & \overline{\boldsymbol{\psi}}_u \\ \boldsymbol{\psi}_q & \overline{\boldsymbol{\psi}}_q \end{bmatrix} = \begin{bmatrix} \boldsymbol{\psi}_u & \overline{\boldsymbol{\psi}}_u \\ \boldsymbol{\psi}_q & \overline{\boldsymbol{\psi}}_q \end{bmatrix}\begin{bmatrix} \boldsymbol{S}_n & * \\ & \boldsymbol{S}_p \end{bmatrix} \tag{13}$$

where $\boldsymbol{\psi}_u, \boldsymbol{\psi}_q, \overline{\boldsymbol{\psi}}_u \text{ and } \overline{\boldsymbol{\psi}}_q$ are transformation matrices and $\boldsymbol{S}_n \text{ and } \boldsymbol{S}_p$ are block-diagonal Schur matrices [11]

For nodal displacement on the boundary of the polygon ($\xi = 1$), c_n in Eq. 11 can be defined

$$\boldsymbol{c}_n = \boldsymbol{\psi}_u^{-1} u_b \tag{14}$$

By substituting Eq. (14) and Eq. (11) into Eq. (2),

$$\boldsymbol{u}(\xi, \eta) = \mathbb{N}_u(\eta) \boldsymbol{\psi}_u \xi^{-S_n} \boldsymbol{\psi}_u^{-1} u_b \tag{15}$$

Hence the scaled boundary shape function for a polygon can be extracted from Eq. (15) as

$$\boldsymbol{\Theta}(\xi, \eta) = \mathbb{N}_u(\eta) \boldsymbol{\psi}_u \xi^{-S_n} \boldsymbol{\psi}_u^{-1} \tag{16}$$

Similarly, the strain-displacement relationship can be obtained by substituting Eq. (15) into Eq. (4)

$$\boldsymbol{\epsilon}(\xi, \eta) = \mathbb{B}(\xi, \eta) \boldsymbol{u}_b \tag{17}$$

where

$$\mathbb{B}(\xi, \eta) = \boldsymbol{\psi}_\epsilon(\eta) \xi^{-S_n - I} \boldsymbol{\psi}_u^{-1} \quad and \quad \boldsymbol{\psi}_\epsilon(\eta) = (\mathbb{B}_1(\eta)\boldsymbol{\psi}_u[-\boldsymbol{S}_n] + \mathbb{B}_2(\eta)\boldsymbol{\psi}_u)$$

Considering virtual work theory, the nonlinear equilibrium of a polygon can be expressed in the form of SBFEM as [11]

$$\int_V \delta\boldsymbol{\epsilon}^T(\xi, \eta) \, \Delta\boldsymbol{\sigma}(\xi, \eta) dV = \int_\Gamma \delta\boldsymbol{u}^T(\xi, \eta) \boldsymbol{f}_t d\Gamma + \int_V \delta\boldsymbol{u}^T(\xi, \eta) \boldsymbol{f}_b dV$$
$$- \int_V \delta\boldsymbol{\epsilon}^T(\xi, \eta) \boldsymbol{\sigma}(\xi, \eta) dV \tag{18}$$

where $\Delta\boldsymbol{\sigma}(\xi, \eta)$ is incremental stress, $\delta\boldsymbol{\epsilon}(\xi, \mu)$ is virtual strain, $\boldsymbol{u}(\xi, \eta)$ is virtual displacement and $\boldsymbol{f}_t \text{ and } \boldsymbol{f}_b$ are surface traction and body load respectively.

Considering stress-strain relationship $\Delta\boldsymbol{\sigma} = \boldsymbol{D}_{ep}\Delta\boldsymbol{\epsilon}$ (where $\boldsymbol{D}_{ep}$ is elastoplastic constitutive matrix) and substituting Eq. (15) and Eq. (17) into Eq. (18), Eq. (18) can be extended into a nonlinear equation as

$$\left(\underbrace{\int_V \mathbb{B}^T(\xi,\eta)\,\boldsymbol{D}_{ep}\mathbb{B}(\xi,\eta)dV}_{\boldsymbol{K}_{ep}}\right)\Delta\boldsymbol{u}_b = \underbrace{\int_\Gamma \boldsymbol{\Theta}^T(\xi,\eta)\boldsymbol{f}_t d\Gamma + \int_V \boldsymbol{\Theta}^T(\xi,\eta)\boldsymbol{f}_b dV}_{\boldsymbol{R}_{ext}}$$

$$-\underbrace{\int_V \mathbb{B}^T(\xi,\eta)\boldsymbol{\sigma}(\xi,\eta)dV}_{\boldsymbol{R}_{int}} \tag{19}$$

$$\boldsymbol{K}_{ep}\Delta\boldsymbol{u}_b = \boldsymbol{R}_{ext} - \boldsymbol{R}_{int} \tag{20}$$

The global system of the equation can be generated by assembling the Eq. (20) for all the polygons, similar to the finite element method. The full derivation of the SBFEM elastoplastic formulation can be referred to in the literature [14]. The Mohr-Coulomb failure criteria has been taken as the failure criterion in this study, while the return mapping method is combined with the modified Newton Rapson method to capture the elastoplastic behaviour of the materials. The initial stress method is used to reduce the computational requirements. Hence, the initial constitutive matrix is calculated at the beginning of the analysis.

2.2 Image-based computational mesh generation

Digital images are formed with tiny squares called pixels arranged in a form of a matrix which can represente information about material properties and distributions with a unique colour. Considering the colour distribution, these pixels recursively split into uniform-coloured squares and create a quadtree mesh overlapping the original image. Hence, the colours that represent the material type or properties can be easily assigned to each corresponding cell in the generated mesh which can be used in the numerical simulation. The MATLAB function 'qtdecomp' is used to generate the quadtree mesh using images. The gradation mesh sizes can be controlled by the user as required for meshing.

In this study, three separate images are considered: the material stratigraphy, spatial variation of cohesion and spatial variation of friction angle, which are used to generate computational mesh. As shown in Figure 2, spatial variable images of cohesion and friction angle have meshed with $2^0 : 2^0$ pixel size elements while material variability image meshes with $2^0 : 2^3$ of the gradient range of element sizes. Since the smallest element size is common to all meshes, all three meshes can overlap as shown in Figure 2. The material parameters are then extracted from each spatial variation mesh and assigned to the corresponding material variability mesh to generate the computational mesh. When several elements overlap with one element in the material variability mesh, the weighted average is taken. The generated computational mesh was then rescaled into actual size to represent the real scale.
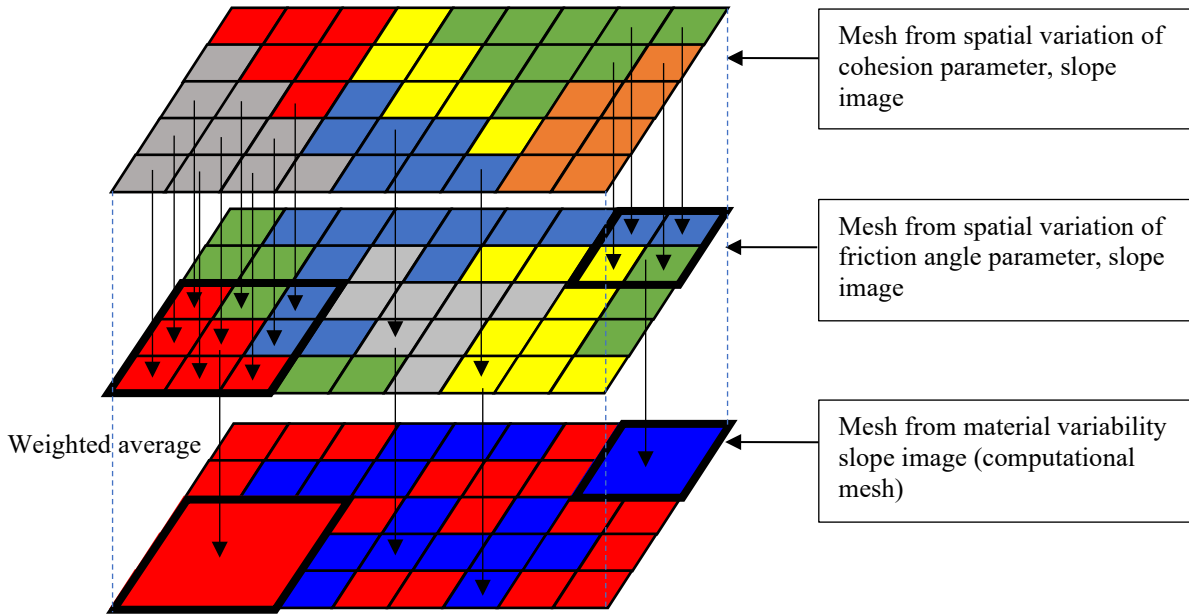
Figure 2: Computational mesh generation

2.3   The factor of safety calculation

In geotechnical and mining engineering, stability of structural design is represented by a quantitative value known as factor of safety (FoS). The shear strength reduction technique and local factor of safety calculation method are used to quantify the stability of a slope. In this study, the strength reduction technique is used to calculate the factor of safety. The shear strength reduction method involves reducing the shear strength parameters iteratively until the failure occurs. Hence, the initial shear strength parameters, initial cohesion ($c_{initial}$) and initial friction ($f_{initial}$) angle are reduce according to

$$c_{effectiv} = \frac{C_{initial}}{SRF} \qquad and \qquad f_{effective} = \frac{f_{initial}}{SRF} \qquad (21)$$

where *SRF* is the strength reduction factor, $c_{effective}$ is the effective cohesion and $f_{effective}$ is the effective friction angle. In this study, non-convergence of the elastoplastic analysis is considered to determine the failure of the slope. The convergence tolerance value is considered as 0.0001 and the iterative ceiling value is considered as 500 [2]. The FoS value is calculated to the accuracy of 0.1 decimal places as it is adequate for large scale open-pit mines.

3   CASE STUDY

Rocks and soils show random variations of their material properties due to factors such as different depositing rates, cooling rates, chemical mixture compositions etc. Hence, consideration of the spatial variation of material parameters is important in geotechnical design. On the other hand, timely analysis of geotechnical designs with the developments such as excavation is important. Hence in this case study, the ability of image-based SBFEM to

effectively integrate spatial variable material parameters of cohesion and friction angle in slope stability analysis while timely modification of the slope geometry easily is demonstrated. Mainly, geomaterial information is obtained from the limited core drillings in the interesting area. Hence to obtain the whole picture of the interesting area, collected data is interpolated according to random field theory [15]. A study of the influence of spatial variation of material parameters of the Yallourn mine was reported [16] and the same spatial correlation lengths of the random field were used in this study to generate spatial variable images as shown in Figure 3a and Figure 3b. The stratigraphy is shown in Figure 3c.
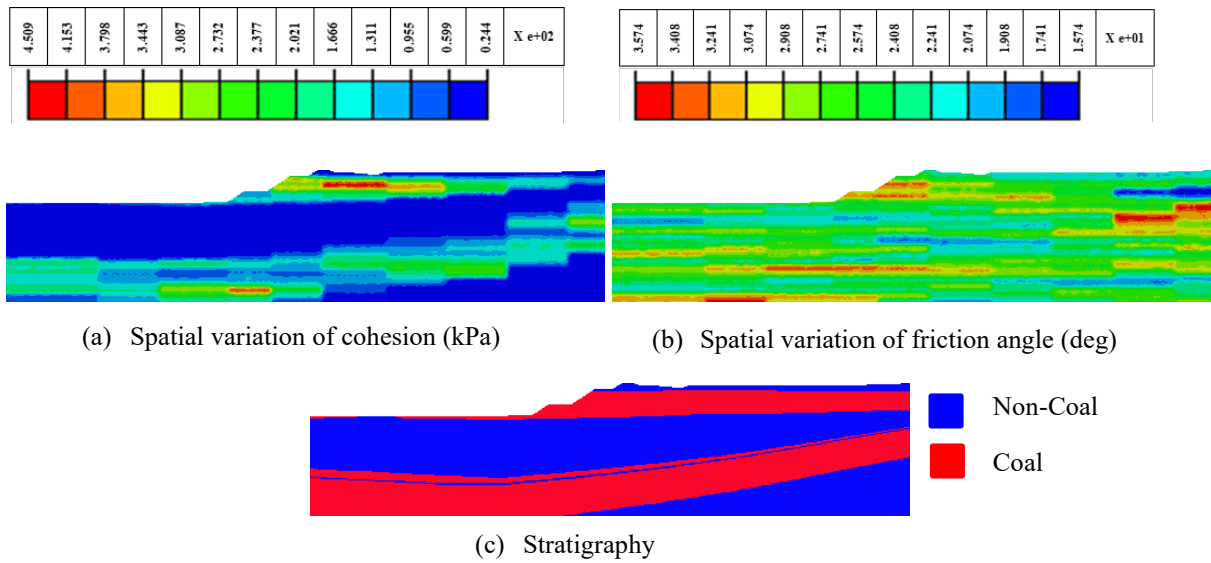

(a) Spatial variation of cohesion (kPa)

(b) Spatial variation of friction angle (deg)

(c) Stratigraphy

Figure 3: Spatial variation of cohesion and friction angle and stratigrapy of the Yallourn mine slope

As described in Section 2.2, the computational mesh was generated combining three images shown in Figure 3. The material properties of coal and non-coal as tabulated in Table 1 were assigned into each corresponding cell according to its colours. The dry condition is considered in this study.

Table 1: Material Properties

Material	Colour of Material	E (kPa)	ν	Friction Angle (°)	Cohesion (kPa)	γ (kN/m³)
Non-coal	Blue	52000	0.3	23.67	31.81	20.15
Coal	Red	40000	0.2	27.28	150.72	11.4
Backfill	Black	42000	0.3	15	32	20

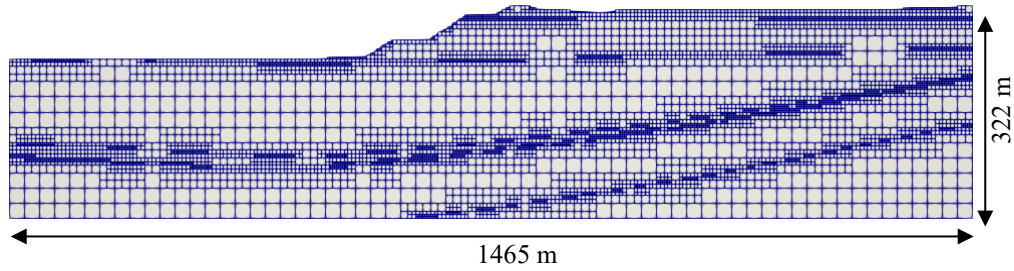The generated computational mesh is shown in Figure 4.

Figure 4: Computational mesh for initial slope geometry

Since input information such as slope geometry and material parameters are given as images, timely modification or development can be simply included only editing the image and analysing the new stage of development. Since the mesh generation is fully automatic, the user is only required to edit the image as introduced into the analysis. To demonstrate this feature of image-based SBFEM, timely excavation of slope and rehabilitation by backfilling at the toe is taken into account as shown in Figure 5.

Figure 5(b and c) show the slope changes due to two stages of coal extraction while Figure 5(d) shows the backfilling at the toe during the rehabilitation. For each stage, the initial stratigraphic image was simply edited and reintroduced into SBFEM elastoplastic analysis through the image meshing technique. The deformation of the slope at each stage are shown in Figure 6.
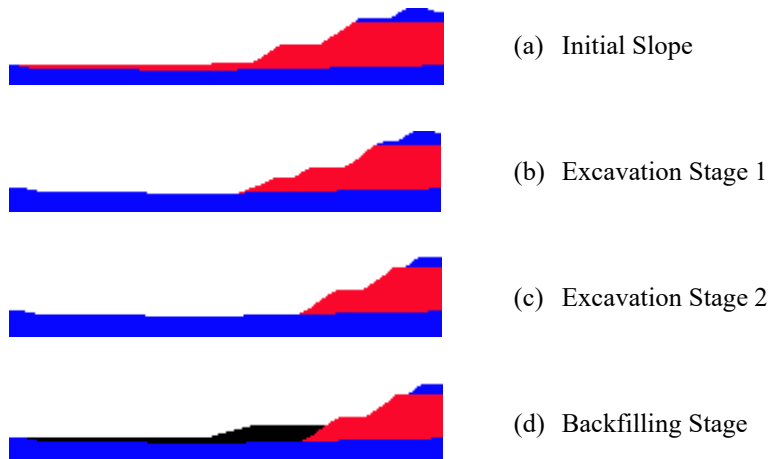

(a) Initial Slope

(b) Excavation Stage 1

(c) Excavation Stage 2

(d) Backfilling Stage

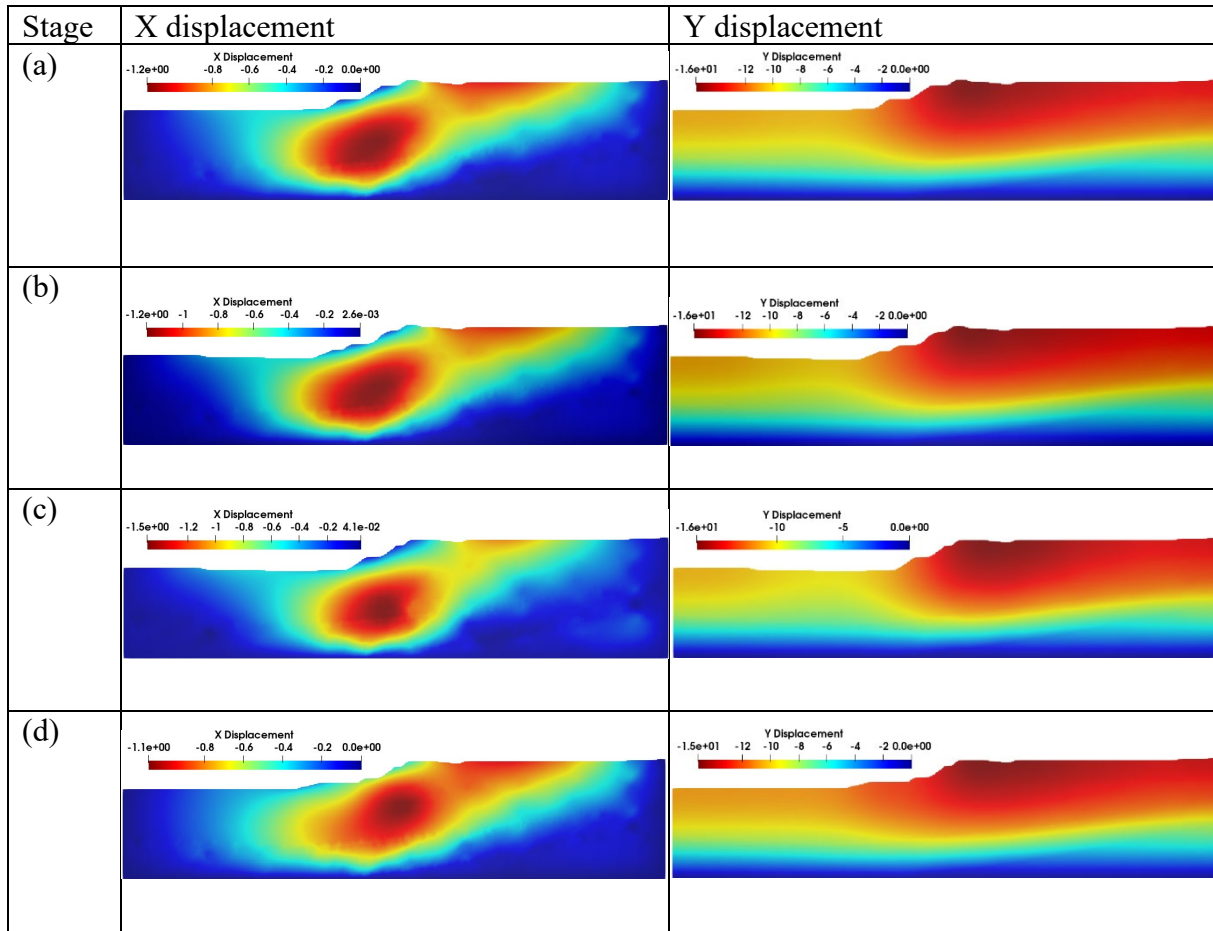**Figure 5**: Timely slope excavations and backfilling

8

Figure 6: X displacement and Y displacement contour maps of four stages

In each stage of the excavation and backfilling, the independent strength reduction method proceeded to calculate the factor of safety while reducing the shear strength parameters iteratively. The failure surface of the slope can be seen in Figure 7. The plastic deformation develops from the toe of the slope to the top of the slope as the slope fails. The FoS value varies with the coal excavation as shown in Figure 8. However, backfilling at the toe enhanced the FoS to a value of 3.6.
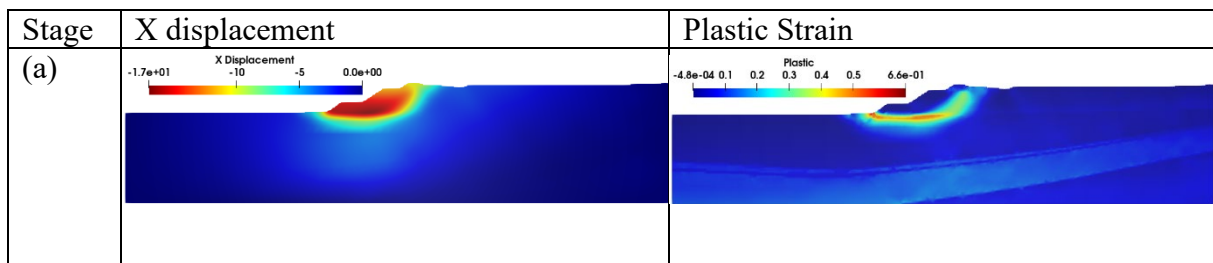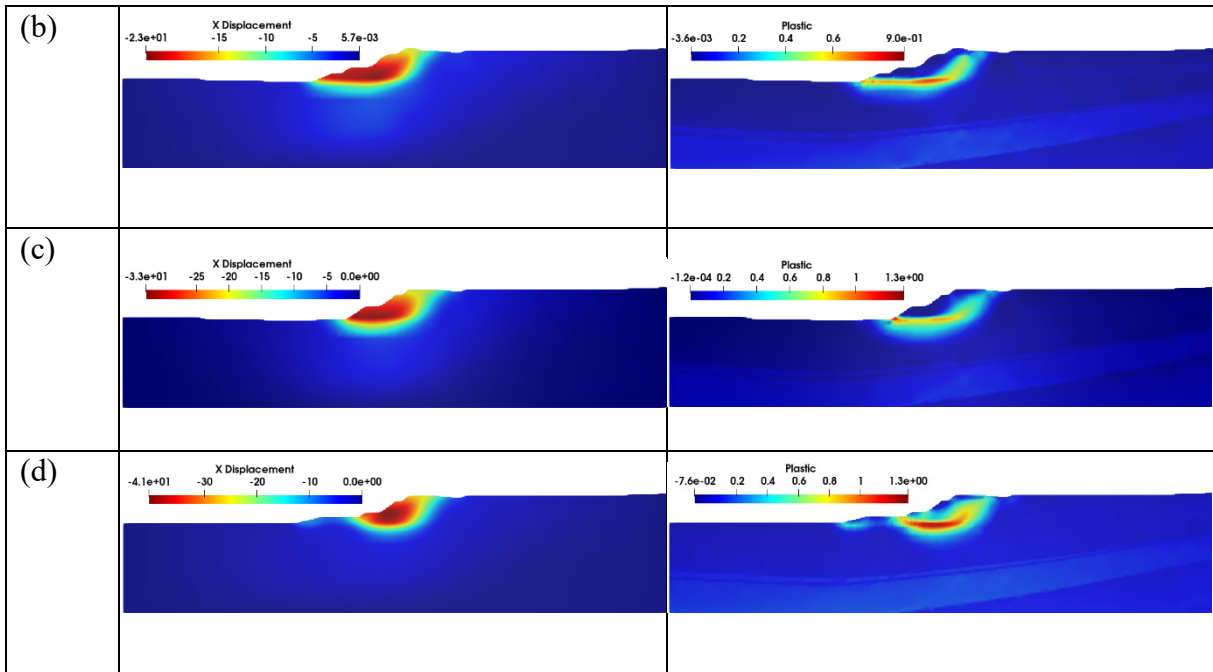
Figure 7: Failure surface and plastic strain contour maps of four stages

According to the shear strength reduction technique, the factor of safety of each stage was calculated and plotted as shown in Figure. 8.
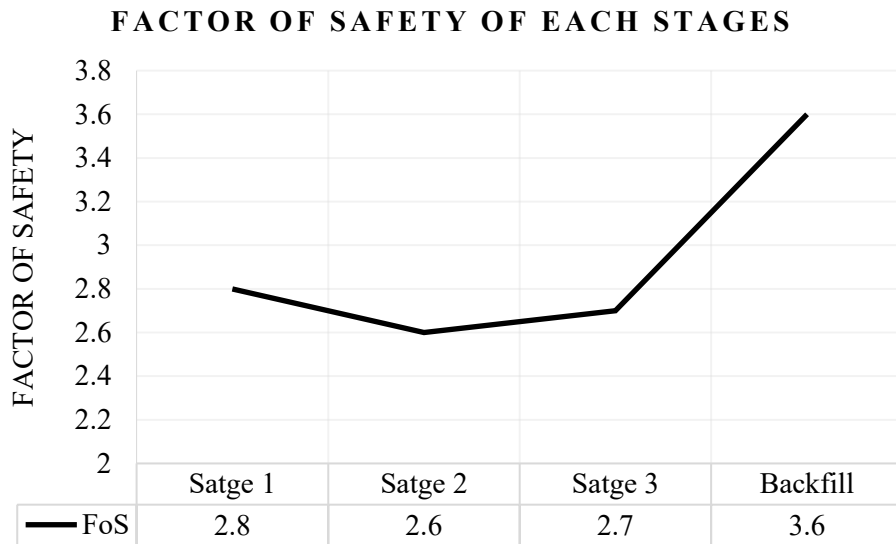

FACTOR OF SAFETY OF EACH STAGES

	Satge 1	Satge 2	Satge 3	Backfill
——FoS	2.8	2.6	2.7	3.6

Figure 8: Factor of safety variation for four stages

4 CONCLUSION

In this study, a numerical technique combining image-based quadtree meshing with the scaled boundary finite element method was used to analyse slope stability. Since the scaled boundary finite element is capable of discretising any size or shape of element, image-based quadtree mesh is easily integrated into the analysis. Hence, complex geological features such as the spatial variability of material parameters and complex geometries can be easily captured and input in the form of images. On the other hand, image-based mesh generation is fully automatic and requires minimum human involvement. Timely modification to the analysis can be easily updated by simply modifying the image.

The Mohr-Coulomb criteria were used as an elasto-plastic constitutive model to analyse the soil behaviour while the return mapping technique combined with the modified Newton's method is used to project the elastoplastic behaviours in an iterative procedure. The initial stress method is used to reduce the computational requirements.

As a case study, a spatial variable slope of the Yallourn mine is used to demonstrate the capabilities of incorporating spatial variabilities in slope stability analysis. The three stages of coal excavation and backfilling stage were analysed with the SBFEM image-based method, with the shear strength reduction technique used to calculate the factor of safety value of each stage.

5 ACKNOWLEDGMENT

6 REFERENCES

[1] Griffiths, D.V. and Lane, P.A., *Slope stability analysis by finite elements.* Geotechnique, 1999. **49**(3): p. 387-403.

[2] Wijesinghe, D.R., et al., *Development of the scaled boundary finite element method for image-based slope stability analysis.* Computers and Geotechnics, 2022. **143**: p. 104586.

[3] Lorig, L. and Varona, P., *Practical slope-stability analysis using finite-difference codes.* Slope stability in surface mining, 2000: p. 115-124.

[4] Bishop, A.W., *The use of the slip circle in the stability analysis of slopes.* Geotechnique, 1955. **5**(1): p. 7-17.

[5] Spencer, E., *A method of analysis of the stability of embankments assuming parallel inter-slice forces.* Geotechnique, 1967. **17**(1): p. 11-26.

[6] Janbu, N. *Application of composite slip surface for stability analysis.* in *Proceedings of European Conference on Stability of Earth Slopes, Sweden, 1954.* 1954.

[7] Allan, F.C., Yacoub, T.E., and Curran, J.H. *On using spatial methods for heterogeneous slope stability analysis.* in *46th US Rock Mechanics/Geomechanics Symposium.* 2012. American Rock Mechanics Association.

[8] Cho, S.E., *Effects of spatial variability of soil properties on slope stability.* Engineering Geology, 2007. **92**(3-4): p. 97-109.

[9] Griffiths, D., Huang, J., and Fenton, G.A., *Influence of spatial variability on slope reliability using 2-D random fields.* Journal of geotechnical and geoenvironmental engineering, 2009. **135**(10): p. 1367-1378.

[10]   Dyson, A.P. and Tolooiyan, A., *Comparative Approaches to Probabilistic Finite Element Methods for Slope Stability Analysis.* Simulation Modelling Practice and Theory, 2020. **100**: p. 102061.

[11]   Song, C., *The Scaled Boundary Finite Element Method: Introduction to Theory and Implementation*. 2018: Wiley. 504.

[12]   Wolf, J.P. and Song, C., *Finite-element modelling of unbounded media*. 1996: Wiley Chichester.

[13]   Deeks, A.J. and Wolf, J.P., *A virtual work derivation of the scaled boundary finite-element method for elastostatics.* Computational Mechanics, 2002. **28**(6): p. 489-504.

[14]   Ooi, E.T., Song, C., and Tin-Loi, F., *A scaled boundary polygon formulation for elasto-plastic analyses.* Computer Methods in Applied Mechanics and Engineering, 2014. **268**: p. 905-937.

[15]   Vanmarcke, E.H., *Probabilistic modeling of soil profiles.* Journal of the geotechnical engineering division, 1977. **103**(11): p. 1227-1246.

[16]   Dyson, A.P. and Tolooiyan, A., *Prediction and classification for finite element slope stability analysis by random field comparison.* Computers and Geotechnics, 2019. **109**: p. 117-129.